# Identification of Material Parameters by Particle Filter Using Observation Data Obtained during Construction of Rock-Fill Dam

**Eiki Tanenaga**, *Kajima Corporation, Tokyo, Japan; email: tanenaga@kajima.com*
**Kazunori Fujisawa**, *Associate Professor, Kyoto University, Kyoto, Japan; email: fujisawa.kazunori.2s@kyoto-u.ac.jp*
**Akira Murakami**, *Professor, Kyoto University, Kyoto, Japan; email: murakami.akira.5u@kyoto-u.ac.jp*

**ABSTRACT**: *When an earth dam is constructed, the mechanical behavior must be monitored in order to realize and confirm the safe construction of the dam. In addition, a numerical analysis is commonly conducted before and during the construction to predict the future behavior of the structure. Often, however, not all the material parameters needed for the numerical analysis are available; parameter identification has therefore been an important problem in numerical simulations performed to predict future behavior. This case study targets a rock-fill dam in the Kyushu area of Japan, and its objectives are to enhance the prediction of dam deformation and to demonstrate the identification of the unknown constitutive parameters needed for the actual dam construction process. The particle filter, incorporated into the soil/water coupled FEM, is used for the parameter identification. The identification results show that the numerical results obtained from the identified parameters agree considerably well with the observation data and that 10,000 particles are sufficient for making an accurate prediction.*

**KEYWORDS:** Data assimilation, Parameter identification, Particle filter, Rock-fill dam

## INTRODUCTION

Dams are typically huge structures constructed with soil materials. During the construction of a soil structure, the mechanical behavior, such as deformation and water pressure, must be monitored in order to achieve and confirm its safe construction. Moreover, it is typical to carry out a numerical analysis before and during the construction to predict the future behavior of the structure. Thus far, several case studies have attempted to numerically simulate the mechanical behavior of such structures by FEM and DEM (e.g., Broojerdi et al., 2018; Aydemir et al., 2017; Kanungo et al., 2013; Kong et al., 2002).

Determining the material parameters, such as the hydraulic conductivity, elastic modulus, and yield stress, is indispensable for predicting the deformation or for performing a risk analysis of soil structures. However, often not all the material parameters needed for the numerical analysis can be obtained. This has been a common problem in numerical simulations performed to predict the future behavior of structures. Although laboratory testing can provide the physical and mechanical properties of soil materials which are the most acceptable for numerical analyses, there are usually several material parameters which are difficult to determine because of the limitations of time, money, and/or experimental techniques, or which suffer from inaccuracy due to differences between the conditions in the laboratory and at the construction site. Hence, the identification of the material parameters has been an important problem in the field of geotechnical engineering as well as dam engineering. For example, there is a study by Schaap et al. (2001) in which a computer program called Rosetta was developed to determine soil hydraulic parameters. Recently, there have also been studies whose purpose was to identify material parameters for constructed dams and the ground (e.g., Huang et al., 2012; Toromanovic et al., 2020; Bhutto et al., 2019). As suggested by Kool et al. (1987), field-scale parameter estimations have been necessary, and there is still sufficient room for improvement in parameter identification for practical application.

Data assimilation is a broad research subject which adjusts numerical models in accordance with observations or measurements. The development of data assimilation has been achieved mainly in the field of geoscience, such as

Submitted: 23 January 2021; Published: 10 December 2021
Reference: Tanenaga E., Fujisawa K., and Murakami A. (2021). Identification of Material Parameters by Particle Filter Using Observation Data Obtained during Construction of Rock-Fill Dam. International Journal of Geoengineering Case Histories, Volume 7, Issue 1, pp. 76-94, doi: 10.4417/IJGCH-07-01-04

oceanography and meteorology, and nowadays it is being applied to various problems in the fields of engineering, medical science, and anthropology (e.g., Nakano et al., 2019; Motesharrei et al., 2016). There are several typical methods for data assimilation, such as the Kalman Filter (KF) for linear problems, and the ensemble Kalman Filter (EnKF; Evensen, 1994; Evensen, 2006) and the Particle Filter (PF; Gordon, 1993; Kitagawa, 1996) for nonlinear problems. These methods enable parameters included in the numerical models to be identified with the aid of observation data. In geotechnical engineering, several previous studies have been done on parameter identification by the methods of data assimilation; for example, Bailey et al. (2010) employed EnKF for estimating the hydraulic conductivity, and Shuku et al. (2012), Murakami et al. (2013), and Nguyen et al. (2015) applied the PF for identifying the parameters of constitutive models.

The objectives of this case study are to enhance the prediction of the deformation of dams in order to achieve their safe construction and to demonstrate the identification of the unknown constitutive parameters needed for the actual construction process. The PF is used for the parameter identification. The next section explains the PF, the constitutive model used for this study, and the numerical analysis of the dam deformation. Then, the results of the parameter identification are presented, followed by the conclusions of this paper.

## METHODOLOGY

### Particle Filter (PF)

The PF is regarded as the nonlinear Kalman filter; it is used as one of the methods for data assimilation. Since the detailed derivation of the PF can be found in Murakami et al. (2013) and Takamatsu et al. (2020), only a brief description of the method via the SIS (Sequential Importance Sampling) algorithm is shown in this section. Generally, data assimilation techniques including the PF need a state space model, which describes the prediction and observation of state variables. The following state space model is capable of describing the mechanical behavior of soil structures, such as dams, with nonlinear stress-strain relationships:

$$\boldsymbol{x}_t = \boldsymbol{f}_t(\boldsymbol{x}_{t-1}) + \boldsymbol{v}_t \tag{1a}$$

$$\boldsymbol{y}_t = \boldsymbol{h}_t(\boldsymbol{x}_t) + \boldsymbol{\varepsilon}_t \tag{1b}$$

where $\boldsymbol{x}_t$, $\boldsymbol{y}_t$, $\boldsymbol{v}_t$, $\boldsymbol{\varepsilon}_t$, $\boldsymbol{f}_t$, and $\boldsymbol{h}_t$ denote the vectors of the state variables, observation data, system noise, observation noise, prediction function, and observation function, respectively. Subscript $t$ or $t$-1 means the time steps in Eq. (1). Function $\boldsymbol{f}_t$ corresponds to the so-called soil-water coupled analysis used to predict the deformation of soil structures. It should be noted that the state vector can include material parameters as well as the variables which are solved in the numerical analysis, such as displacement and pore water pressure. The system and observation noises are commonly assumed to follow the normal distribution.

$$\boldsymbol{v}_t \sim N(0, \boldsymbol{Q}_t) \tag{2a}$$

$$\boldsymbol{\varepsilon}_t \sim N(0, \boldsymbol{R}_t) \tag{2b}$$

The basic purpose of the PF is to obtain the following conditional probabilistic density function $p(\boldsymbol{x}_t|\boldsymbol{y}_{1:t})$, called the posterior distribution, when the nonlinear state space model is employed. Bayes' theorem develops posterior distribution $p(\boldsymbol{x}_t|\boldsymbol{y}_{1:t})$ into the following form:

$$p(\boldsymbol{x}_t|\boldsymbol{y}_{1:t}) = \frac{p(\boldsymbol{y}_t|\boldsymbol{x}_t, \boldsymbol{y}_{1:t-1})\, p(\boldsymbol{x}_t|\boldsymbol{y}_{1:t-1})}{p(\boldsymbol{y}_t|\boldsymbol{y}_{1:t-1})} \tag{3}$$

In the numerator of Eq. (3), $p(\boldsymbol{x}_t|\boldsymbol{y}_{1:t-1})$ and $p(\boldsymbol{y}_t|\boldsymbol{x}_t, \boldsymbol{y}_{1:t-1})$ are determined by the prediction equation, Eq. (1a), and the observation equation, Eq. (1b), respectively. The denominator has the normalization constants, which can be obtained by:

$$p(\boldsymbol{y}_t|\boldsymbol{y}_{1:t-1}) = \int p(\boldsymbol{y}_t|\boldsymbol{x}_t, \boldsymbol{y}_{1:t-1})\, p(\boldsymbol{x}_t|\boldsymbol{y}_{1:t-1})\, d\boldsymbol{x}_t \tag{4}$$

At time step *t*-1, probabilistic density distribution $p(\boldsymbol{x}_{t-1}|\boldsymbol{y}_{1:t-1})$ is given. The PF aproximates it in the following form with the aid of the ensemble $\left\{\boldsymbol{x}_{t-1|t-1}^{(i)}\right\}_{i=1}^{N}$ composed by N samples of $\boldsymbol{x}_{t-1|t-1}^{(i)}$. Each sample of $\boldsymbol{x}_{t-1|t-1}^{(i)}$ is called a "particle".

$$p(\boldsymbol{x}_{t-1}|\boldsymbol{y}_{1:t-1}) \approx \sum_{i=1}^{N} w_{t-1}^{(i)} \delta(\boldsymbol{x}_{t-1} - \boldsymbol{x}_{t-1|t-1}^{(i)}) \tag{5}$$

where $\delta$ is Dirac's delta function and $w_{t-1}^{(i)}$ is the weight of the *i*th particle. Given the ensemble approximation of $p(\boldsymbol{x}_{t-1}|\boldsymbol{y}_{1:t-1})$, $p(\boldsymbol{x}_t|\boldsymbol{y}_{1:t-1})$ can be transformed as follows:

$$\begin{aligned} p(\boldsymbol{x}_t|\boldsymbol{y}_{1:t-1}) &= \int p(\boldsymbol{x}_t|\boldsymbol{x}_{t-1}, \boldsymbol{y}_{1:t-1})\, p(\boldsymbol{x}_{t-1}|\boldsymbol{y}_{1:t-1})\, d\boldsymbol{x}_t \\ &= \int p(\boldsymbol{x}_t|\boldsymbol{x}_{t-1}) \sum_{i=1}^{N} w_{t-1}^{(i)} \delta(\boldsymbol{x}_{t-1} - \boldsymbol{x}_{t-1|t-1}^{(i)})\, d\boldsymbol{x}_t \\ &= \sum_{i=1}^{N} \int w_{t-1}^{(i)} \delta(\boldsymbol{x}_{t-1} - \boldsymbol{x}_{t-1|t-1}^{(i)}) p(\boldsymbol{x}_t|\boldsymbol{x}_{t-1})\, d\boldsymbol{x}_t \\ &= \sum_{i=1}^{N} w_{t-1}^{(i)} p\left(\boldsymbol{x}_t|\boldsymbol{x}_{t-1|t-1}^{(i)}\right) \\ &= \sum_{i=1}^{N} w_{t-1}^{(i)} \delta(\boldsymbol{x}_t - \boldsymbol{x}_{t|t-1}^{(i)}) \end{aligned} \tag{6}$$

where

$$\boldsymbol{x}_{t|t-1}^{(i)} = \boldsymbol{f}(\boldsymbol{x}_{t-1|t-1}^{(i)}) + \boldsymbol{v}_t^{(i)} \tag{7}$$

$p(\boldsymbol{y}_t|\boldsymbol{x}_t, \boldsymbol{y}_{1:t-1})$ is called the likelihood and can be directly obtained from Eqs. (1b) and (2b).

$$p(\boldsymbol{y}_t|\boldsymbol{x}_t, \boldsymbol{y}_{1:t-1}) = p(\boldsymbol{y}_t|\boldsymbol{x}_t) = \frac{1}{\sqrt{(2\pi)^m |R_t|}} \exp\left[-\frac{\left(\boldsymbol{y}_t - \boldsymbol{h}_t(\boldsymbol{x}_t)\right)^T R_t^{-1} \left(\boldsymbol{y}_t - \boldsymbol{h}_t(\boldsymbol{x}_t)\right)}{2}\right] \tag{8}$$

Substituting Eqs. (6) and (8) into Eq. (4), the denominator of Eq. (3) is reduced to the following form:

$$p(\boldsymbol{y}_t|\boldsymbol{y}_{1:t-1}) = \sum_{i=1}^{N} w_{t-1}^{(i)} p\left(\boldsymbol{y}_t|\boldsymbol{x}_{t|t-1}^{(i)}\right) \tag{9}$$

Substituting Eqs. (6), (8), and (9) into Eq. (3), the posterior probabilistic density function $p(\boldsymbol{x}_t|\boldsymbol{y}_{1:t})$ becomes:

$$p(\boldsymbol{x}_t|\boldsymbol{y}_{1:t}) = \sum_{i=1}^{N} w_t^{(i)}\, \delta(\boldsymbol{x}_t - \boldsymbol{x}_{t|t}^{(i)}) \tag{10}$$

Where

$$w_t^{(i)} = \frac{p\left(\boldsymbol{y}_t|\boldsymbol{x}_{t|t-1}^{(i)}\right) w_{t-1}^{(i)}}{\sum_{j=1}^{N} w_{t-1}^{(j)} p\left(\boldsymbol{y}_t|\boldsymbol{x}_{t|t-1}^{(j)}\right)} \quad , \quad \boldsymbol{x}_{t|t}^{(i)} = \boldsymbol{x}_{t|t-1}^{(i)} \tag{11}$$

The second equation in Eq. (11) is available only when the SIS algorithm is employed. In the SIS algorithm, the weight $w_t^{(i)}$ of each particle is updated without resampling, as seen in Eq. (11).

The algorithm of the PF, shown in Eqs. (3)-(11), is simply summarized as seen below.

1. Prepare the initial set of particles $\left\{\boldsymbol{x}_{0|0}^{(i)}\right\}_{i=1}^{N}=\left[\boldsymbol{x}_{0|0}^{(1)},\ldots,\boldsymbol{x}_{0|0}^{(N)}\right]$ with the initial weight of $\left\{\boldsymbol{w}_{0}^{(i)}\right\}_{i=1}^{N}=\left[\boldsymbol{w}_{0}^{(1)},\ldots,\boldsymbol{w}_{0}^{(N)}\right]$.

2. When $t$=1, …, $T$, calculate $\boldsymbol{x}_{t|t-1}^{(i)}$ ($i$=1, …, $N$) as

$$\boldsymbol{x}_{t|t-1}^{(i)}=\boldsymbol{f}_t(\boldsymbol{x}_{t-1|t-1}^{(i)})+\boldsymbol{v}_t^{(i)} \tag{12}$$

3. Update $\boldsymbol{x}_{t-1|t-1}^{(i)}$ and $\boldsymbol{w}_{t-1}^{(i)}$ ($i$=1, …, $N$) according to Eq. (11), as follows:

$$w_t^{(i)}=\frac{p\left(\boldsymbol{y}_t|\boldsymbol{x}_{t|t-1}^{(i)}\right)w_{t-1}^{(i)}}{\sum_{j=1}^{N}w_{t-1}^{(j)}p\left(\boldsymbol{y}_t|\boldsymbol{x}_{t|t-1}^{(j)}\right)}\ ,\quad \boldsymbol{x}_{t|t}^{(i)}=\boldsymbol{x}_{t|t-1}^{(i)}$$

4. Return to the second step with $t$=$t$+1.

**Constitutive Model for Elasto-plastic Deformation Analysis**

A soil/water coupled elasto-(visco-)plastic finite element analysis, based on DACSAR (Iizuka and Ohta, 1987), is conducted to predict the deformation of a rock-fill dam. The constitutive model originally installed in DACSAR is the so-called Sekiguchi / Ohta model (Sekiguchi and Ohta, 1997). The constitutive model can deal with the mechanical behavior of time dependency, such as secondary consolidation, creep, and stress relaxation, as well as the plastic strain occurring along with anisotropy. The rotation of principal stress can also be considered. Flow surface $F$ is defined as:

$$F=\alpha\ln\left\{1+\frac{\dot{v}_0}{\alpha}\exp\left(\frac{f(\boldsymbol{\sigma}')}{\alpha}\right)\right\}-\varepsilon_v^{vp}=0 \tag{13}$$

which includes yield function $f(\boldsymbol{\sigma}')$ and describes the time-dependent visco-plastic behavior. In Eq. (13), $\alpha$ is the coefficient of secondary consolidation, $\dot{v}_0$ is the initial volumetric strain rate, $f(\boldsymbol{\sigma}')$ is a scalar function corresponding to the yield function, $\boldsymbol{\sigma}'$ is the effective stress tensor, and $\varepsilon_v^{vp}$ is the visco-plastic volumetric strain. Yield function $f(\boldsymbol{\sigma}')$ of the Sekiguchi / Ohta model is defined as follows:

$$f(\boldsymbol{\sigma}')=MD\ln\frac{p'}{p'_0}+D\eta^* \tag{14}$$

where

$$\eta^*=\sqrt{\frac{3}{2}}\|\boldsymbol{\eta}-\boldsymbol{\eta}_0\|\ ,\ \boldsymbol{\eta}=\frac{\boldsymbol{s}}{p'}\ ,\ \boldsymbol{s}=\boldsymbol{\sigma}'-p'\mathbf{1}\ ,\ \boldsymbol{\eta}_0=\frac{\boldsymbol{s}_0}{p'_0}\ ,\ \boldsymbol{s}=\boldsymbol{\sigma}'_0-p'_0\mathbf{1}\ ,\ p'=\frac{1}{3}\boldsymbol{\sigma}':\mathbf{1}\ ,\ p'_0=\frac{1}{3}\boldsymbol{\sigma}'_0:\mathbf{1} \tag{15}$$

$M$ is the critical stress ratio, $D$ is the coefficient of dilatancy, $p'$ is the mean effective stress, $p'_0$ is the mean effective stress in pre-consolidation, $\eta^*$ is the stress ratio parameter, $\boldsymbol{\sigma}'_0$ is the effective stress tensor in pre-consolidation, and $\mathbf{1}$ is the identity tensor.

In previous studies, such as Sun et al. (2004), Zhang and Ai (2012), and Salma et al. (2018), the above Sekiguchi / Ohta model was used for computing the elasto-plastic deformation. However, the yield surface has a singular point under the $K_0$ consolidation condition (See Figure 1). Then, the plastic strain rate cannot be calculated precisely by the associated flow rule because the yield function is not differentiable (Murakami, 2012). In order to avoid this problem, another yield function based on the modified Cam-Clay model is employed, as given below:

$$f(\boldsymbol{\sigma}')=MD\ln\frac{p'}{p'_0}+MD\ln\left(\frac{M^2+\eta^{*2}}{M^2}\right) \tag{16}$$

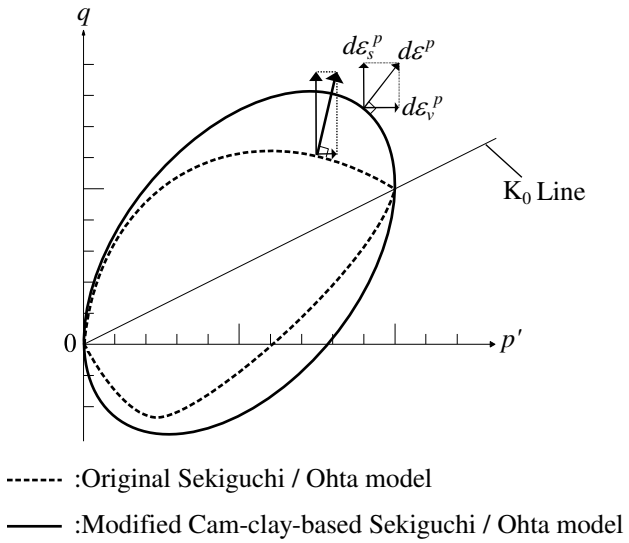


*Figure 1. Yield surface based on modified Cam-C.lay model.*

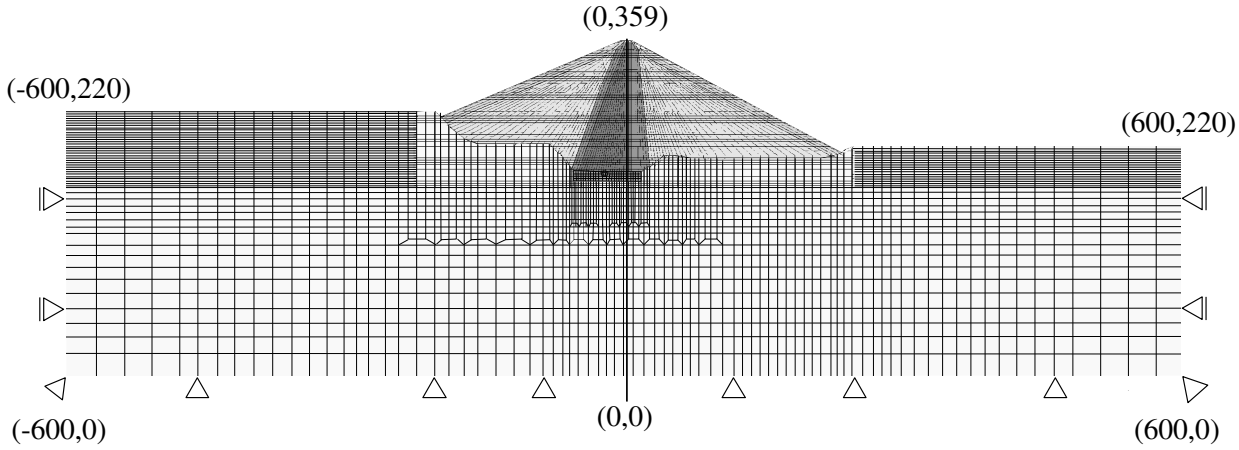


*Figure 2. Finite element mesh of foundation and dam body (Unit: m).*

**Numerical Simulation of Dam during Construction**

The rock-fill dam targeted in this paper is located in the Kyushu Region of Japan. The dam body has already been constructed and is going through the initial impoundment. The deformation of the dam was monitored during its construction and the mechanical behavior was numerically simulated for its safe construction, even though some material parameters were not available *a priori*. This section presents the numerical results, which were achieved through the accurate prediction of the dam deformation and the estimation of the unknown material parameters by means of the PF. Figure 2 shows the finite element mesh of the dam after its embankment had been completely constructed. The finite element mesh has 7,120 elements and 7,208 nodes. The soil/water coupled analysis explained in the previous section is applied to this problem, in which the displacement and the pore water pressure of the dam body are the variables to be solved.

Table 1 lists the material parameters of the core zones. Compression index $\lambda$ and swelling index $\kappa$ were obtained from the slope of the *e*-log*p'* curve in the natural logarithm. The indices calculated in the base-10 logarithm are written as $C_c$ and $C_s$, respectively, and the equalities of $\lambda = 0.434C_c$ and $\kappa = 0.434C_s$ hold true for these indices. There are two types of core zones, the 1st core zone and the 2nd core zone, as shown in the table. The soil materials used for the 1st and 2nd core zones of the dam construction correspond to the zones located below and above EL. 247.00 m, respectively.

*Table 1. Material constants of core zones.*

| Property | Unit | 1st Core Zone | 2nd Core Zone |
|---|---|---|---|
| Wet density $\rho_t$ | t/m$^3$ | 2.241 | 2.256 |
| Void ratio at yield $e_0$ | - | 0.437 | 0.496 |
| Angle of shear resistance $\phi'$ | deg | 33.9 | 34.6 |
| Critical stress ratio $M$ | - | 1.37 | 1.40 |
| Compression index $\lambda$ | - | 0.04166 | 0.03863 |
| Swelling index $\kappa$ | - | 0.00781 | 0.00651 |
| Vertical yield stress $\sigma'_{v0}$ | kPa | 300.0 | 300.0 |
| Poisson's ratio $\nu$ | - | 0.307 | 0.302 |
| Coefficient of earth pressure at rest $K_0$ | - | 0.442 | 0.432 |
| Hydraulic conductivity $k$ | cm/s | $6.6 \times 10^{-7}$ | $1.4 \times 10^{-6}$ |
| Change ratio of hydraulic conductivity $\delta_k$ | - | 0.0319 | 0.0347 |

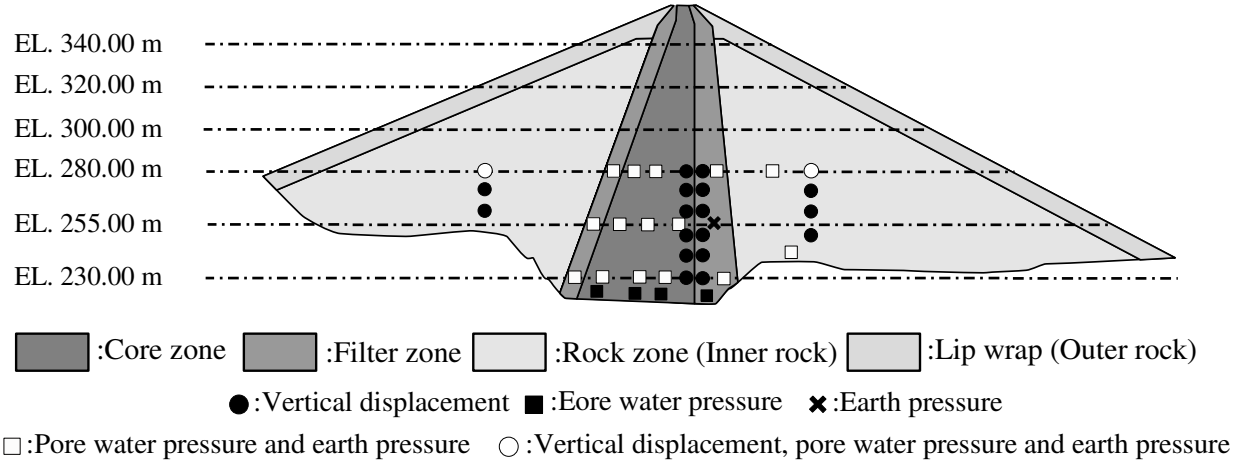


*Figure 3. Cross section of dam and the location of displacement and pressure gauges.*

The soil properties shown in Table 1 were obtained from laboratory testing conducted at the construction site. The density $\rho_t$ was determined by the standard compaction test for the purpose of controlling the compaction work. The friction angle $\phi'$ and the hydraulic coefficient $k$ were obtained from the consolidated-undrained triaxial test and the permeability test, respectively. The critical stress ratio M, the coefficient of earth pressure at rest $K_0$, and the Poisson's ratio $\nu$ were evaluated from the friction angle with the aid of the following relationships: $M=6\sin\phi'/(3-\phi')$, $K_0=1-\sin\phi'$, and $\nu=K_0/(1+K_0)$. The compression index $C_c$ and the swelling index $C_s$ as well as $e_0$, $\sigma'_{v0}$, and $\delta_k$ were obtained from the consolidation test.

Table 2 lists the material parameters of the filter and the rock zones similarly to Table 1. The rock zone is divided into two zones of inner rock and outer rock. The outer rock was utilized for the lip wrap zone covering the inner rock zone (see Figure 3). Comparing Table 1 for the core zones with Table 2 for the filter and rock zones, it is clear that the compression index ($\lambda$ or $C_c$), swelling index ($\kappa$ or $C_s$), and vertical yield stress $\sigma'_{v0}$ are not listed in Table 2. This is because these material constants of the filter and rock zones were unknown and needed to be identified. Although the values of the material constants for these two rock zones are slightly different between the inner and outer zones, the materials for both zones were brought from the same location. Hence, the three parameters are also assumed to be the same for both zones.

In the two-dimensional soil/water coupled analysis used to compute the deformation of the dam, the vertical displacement at the bottom and the horizontal displacement at the side of the foundation were fixed, and the stress-free condition was imposed on the surfaces of the foundation and the embankment. The finite elements of each embankment layer were piled up in accordance with the construction history in order to compute the consolidation process of the constructed embankment layers (See Figure 4). The pore water pressure was computed only in the core and filter zones; the atmospheric pressure was given to the other zones. The foundation was assumed to be linear elastic with the elastic modulus of 1,400 MPa and Poisson's ratio of 0.3.

The vertical displacement (settlement), pore water pressure, and earth pressure were acquired by settlement gages, pressure transducers, and earth pressure gauges once a day for 456 days after the start of the dam construction. The positions of the observation points are shown in Figure 3. Figure 4 presents the cross-sectional mesh of the dam under construction up to the 456th day. It should be noted that the dam had not been completely constructed by the time this study was started. Hence, all the observation points for the settlement, pore water pressure, and earth pressure are located under EL. 280.00 m. In total, there are 19 points for displacement, 22 points for pore water pressure, and 19 points for earth pressure. Moreover, the day on which the data acquisition was begun differs depending on the positions of the observation points, which means that the amount of observation data also differs depending on their positions.

*Table 2. Material constants of filter and rock zones.*

| Property | Unit | Filter | Inner Rock | Outer Rock |
|---|---|---|---|---|
| Wet density $\rho_t$ | t/m$^3$ | 2.364 | 2.263 | 2.286 |
| Void ratio at yield $e_0$ | - | 0.193 | 0.203 | 0.203 |
| Angle of shear resistance $\phi'$ | deg | 39.4 | 43.3 | 43.3 |
| Critical stress ratio $M$ | - | 1.610 | 1.780 | 1.780 |
| Poisson's ratio $\nu$ | - | 0.412 | 0.412 | 0.412 |
| Coefficient of earth pressure at rest $K_0$ | - | 0.700 | 0.700 | 0.700 |
| Hydraulic conductivity $k$ | cm/s | $3.7 \times 10^{-2}$ | $2.6 \times 10^{-1}$ | $5.3 \times 10^{-1}$ |
| Change ratio of hydraulic conductivity $\delta_k$ | - | 0.0061 | 0.0373 | 0.0373 |

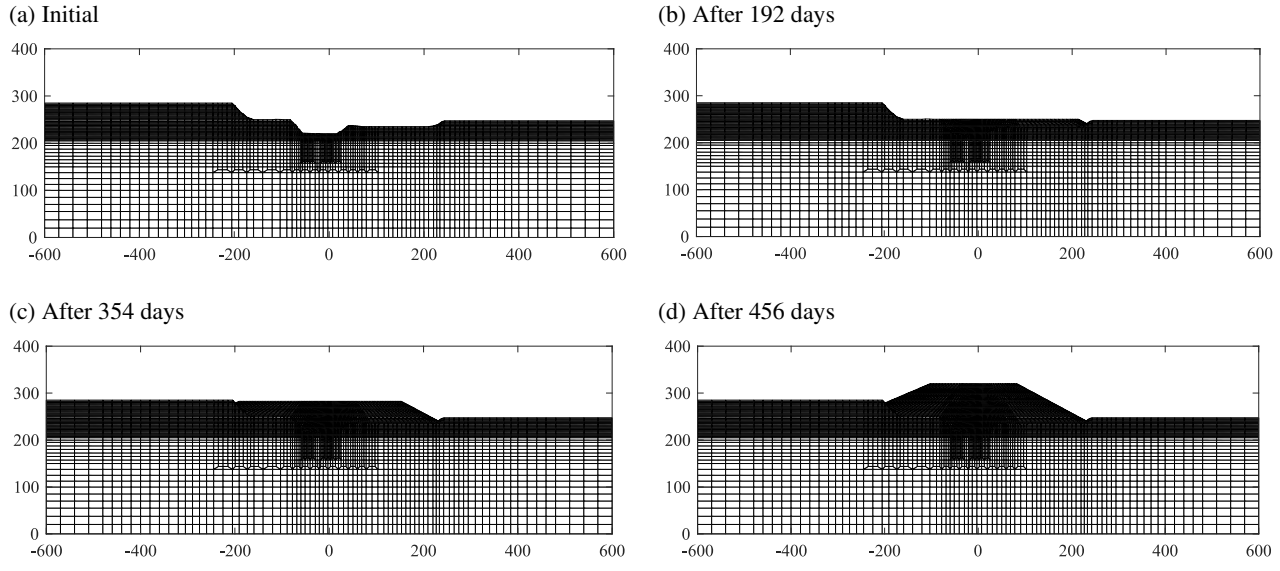


*Figure 4. Cross sections of dam during construction (Unit: m).*

**Procedure for Parameter Identification by Particle Filter**

The procedure for identifying material parameters $C_c$, $C_s$, and $\sigma'_{v0}$ for the filter and rock zones is summarized into the following steps. (The number of parameters to be identified is six.)

*Step 1* (Initialization)**:** Enough sets of six uniform random numbers are generated for making the sets of six parameters in the ranges shown in Table 3. (Each set of six parameters corresponds to a particle.) These ranges were determined according to the empirical data which had been used for the construction of the dam. This step corresponds to the preparation of the initial set of particles $\left\{\boldsymbol{x}_{0|0}^{(i)}\right\}_{i=1}^{N}$. It should be noted that state variable $\boldsymbol{x}$ is the vector having the components of the displacements and the pore water pressure at all the nodal points and the six parameters to be identified. The initial weight $\boldsymbol{w}_0^{(i)}$ of every particle can be assumed to be 1/*N* because uniform random numbers have been given to the six parameters.

*Table 3. Ranges in parameters to be identified.*

| Parameter | $C_c$ | $C_s$ | $\sigma'_{v0}$ |
|---|---|---|---|
| Filter zone | 0.030-0.070 | 0.005-0.015 | 300.0-700.0 |
| Rock zone | 0.043-0.100 | 0.013-0.032 | 400.0-800.0 |

*Step 2* (Prediction): Given each set of parameters, the deformation analysis of the dam is conducted, and the vertical displacement and pore water pressure are solved, which results in $\left\{\boldsymbol{x}_{t|t}^{(i)}\right\}_{i=1}^{N}$ at $t$=1, …, $T$ by recursive use of the following equations in Eqs. (11) and (12):

$$\boldsymbol{x}_{t|t-1}^{(i)} = \boldsymbol{f}(\boldsymbol{x}_{t-1|t-1}^{(i)}) + \boldsymbol{v}_t^{(i)} \ , \ \boldsymbol{x}_{t|t}^{(i)} = \boldsymbol{x}_{t|t-1}^{(i)}$$

In this step, function $\boldsymbol{f}_t$ corresponds to the operation of the soil-water coupled analysis with a set of the parameters given by each particle. For simplicity, system noise $\boldsymbol{v}_t$ was assumed to be zero in order to avoid the determination of the system noise (e.g., Murakami et al., 2013; Takamatsu et al., 2020). However, it should be noted that the uncertainty involved with the state equation is included in the observation noise because the observation noise implies the gap between the prediction by the state equation and the observation.

*Step 3* (Filtering): The weights of the particles $\left\{\boldsymbol{w}_t^{(i)}\right\}_{i=1}^{N}$ can be updated at $t$=1, …, $T$ by recursive use of the following equations derived from Eqs. (8) and (11):

$$w_t^{(i)} = \frac{p\left(\boldsymbol{y}_t|\boldsymbol{x}_{t|t-1}^{(i)}\right) w_{t-1}^{(i)}}{\sum_{j=1}^{N} w_{t-1}^{(j)} p\left(\boldsymbol{y}_t|\boldsymbol{x}_{t|t-1}^{(j)}\right)} \ , \ p\left(\boldsymbol{y}_t|\boldsymbol{x}_{t|t-1}^{(i)}\right) = \frac{1}{\sqrt{(2\pi)^m |R_t|}} \exp\left[-\frac{\left(\boldsymbol{y}_t - \boldsymbol{h}_t\left(\boldsymbol{x}_{t|t-1}^{(i)}\right)\right)^T R_t^{-1}\left(\boldsymbol{y}_t - \boldsymbol{h}_t\left(\boldsymbol{x}_{t|t-1}^{(i)}\right)\right)}{2}\right]$$

Here, $\boldsymbol{h}_t$ corresponds to the operation which outputs the vertical displacement, pore water pressure, and earth pressure at the observation points from a particle $\boldsymbol{x}_{t|t-1}^{(i)}$ (=$\boldsymbol{x}_{t|t}^{(i)}$). In this step, the ensemble approximation of the posterior distribution, $(\boldsymbol{x}_t|\boldsymbol{y}_{1:t}) = \sum_{i=1}^{N} w_t^{(i)} \delta(\boldsymbol{x}_t - \boldsymbol{x}_{t|t}^{(i)})$, can be obtained at every time step.

*Step 4* (Identification): Considering that the state variable vector includes the parameters to be identified, the parameters are identified by averaging the state variable at the final time step ($t$=$T$), as follows:

$$\overline{\boldsymbol{x}}_T = \int \boldsymbol{x}_T p(\boldsymbol{x}_T|\boldsymbol{y}_{1:T})\, d\boldsymbol{x}_T = \int \boldsymbol{x}_T \sum_{i=1}^{N} w_T^{(i)} \delta(\boldsymbol{x}_T - \boldsymbol{x}_{T|T}^{(i)}) d\boldsymbol{x}_T = \sum_{i=1}^{N} w_T^{(i)} \boldsymbol{x}_{T|T}^{(i)} \tag{17}$$

where $\overline{\boldsymbol{x}}_T$ denotes the mean of $\boldsymbol{x}_T$.

In the above procedures, the prediction step (*Step 2*) and the filtering step (*Step 3*) can be completely separated, which is a great advantage of the PF via SIS (Sequential Importance Sampling). Hence, the above procedure is feasible without changing the available computer programs for the numerical simulation at the prediction step. The variance/covariance matrix $R_t$, which is necessary for *Step 3*, was determined as follows (Shuku et al., 2012):

$$R_t = \begin{bmatrix} (\alpha_1 S_1)^2 & 0 & \cdots & \cdots & 0 \\ 0 & (\alpha_2 S_2)^2 & 0 & \cdots & \vdots \\ \vdots & 0 & \ddots & 0 & \vdots \\ \vdots & \vdots & 0 & \ddots & 0 \\ 0 & 0 & \cdots & \cdots & (\alpha_{obs} S_{obs})^2 \end{bmatrix} \tag{18}$$

where $S_1$, $S_2$, … or $S_{obs}$ denotes the maximum value of the measured data at each observation point, and $\alpha_1$, $\alpha_2$, … or $\alpha_{obs}$ denotes the factor for the maximum value. In the following section, the value of 1.7 is given equally to $\alpha_1$, $\alpha_2$, … and $\alpha_{obs}$ in order to avoid serious degeneracy (small variance or covariance of the observation noise easily induce severe degeneracy). The accuracy of the numerical simulation is investigated in terms of the RMSE (Root Mean Square Error) (Chai and Draxler, 2014) between the measured data and the numerical results obtained with the identified parameters.

*Table 4. Parameters identified with different numbers of particles.*

| Number of Particles | Filter Zone | | | Rock Zone | | |
|---|---|---|---|---|---|---|
| | $C_c$ | $C_s$ | $\sigma'_{vo}$ | $C_c$ | $C_s$ | $\sigma'_{vo}$ |
| 2,000 | 0.0522 | 0.0102 | 428.1 | 0.0542 | 0.0151 | 750.4 |
| 3,000 | 0.0522 | 0.0102 | 428.1 | 0.0542 | 0.0151 | 750.4 |
| 4,000 | 0.0522 | 0.0102 | 428.1 | 0.0542 | 0.0151 | 750.4 |
| 5,000 | 0.0516 | 0.0103 | 428.7 | 0.0540 | 0.0150 | 746.7 |
| 6,000 | 0.0515 | 0.0103 | 432.8 | 0.0542 | 0.0149 | 746.0 |
| 7,000 | 0.0515 | 0.0104 | 436.1 | 0.0539 | 0.0148 | 745.4 |
| 8,000 | 0.0514 | 0.0103 | 437.5 | 0.0539 | 0.0147 | 744.2 |
| 9,000 | 0.0512 | 0.0100 | 434.9 | 0.0533 | 0.0146 | 741.9 |
| 10,000 | 0.0512 | 0.0101 | 436.6 | 0.0534 | 0.0146 | 741.4 |
| 11,000 | 0.0510 | 0.0100 | 434.7 | 0.0536 | 0.0145 | 741.0 |
| 12,000 | 0.0510 | 0.0100 | 436.9 | 0.0536 | 0.0145 | 741.2 |
| 13,000 | 0.0506 | 0.0101 | 434.2 | 0.0536 | 0.0144 | 740.1 |
| 14,000 | 0.0505 | 0.0101 | 434.6 | 0.0536 | 0.0144 | 739.0 |
| 15,000 | 0.0504 | 0.0100 | 434.2 | 0.0537 | 0.0143 | 738.6 |

## RESULTS AND DISCUSSION

15,000 particles were generated for the identification of the six material parameters by the PF incorporated into the soil/water coupled analysis. Generally, the number of particles directly affects the accuracy of the identification. The more particles prepared, the better the parameter identification or the better prediction that can be achieved. Table 4 lists the values of the identified parameters along with the different numbers of particles. The recomputed displacement, pore water pressure, and earth pressure are shown in the following figures, i.e., Figures 5 to 20, using the parameters identified with 15,000 particles. In these figures, the solid lines indicate the measured data, while the broken lines indicate the numerical results. It can be seen from these figures that the numerical results reproduce the observed data surprising well. In particular, the numerical results for the displacement, pore water pressure, and earth pressure in the core zones agree fairly well with the measured data. The measured pore water pressure in the filter zone suddenly increased in July of 2018; however, the computation cannot follow this behavior. This numerical analysis adds embankment layers and computes the consolidation. Hence, the aforementioned sudden increase in pore water pressure is not predictable.

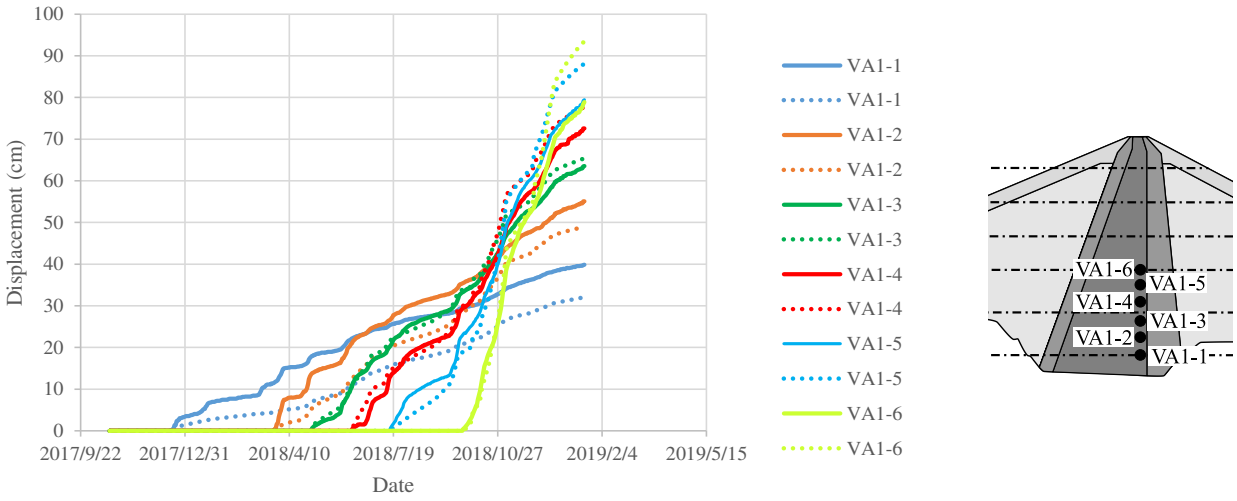


*Figure 5. Time histories of displacement (core zone).*

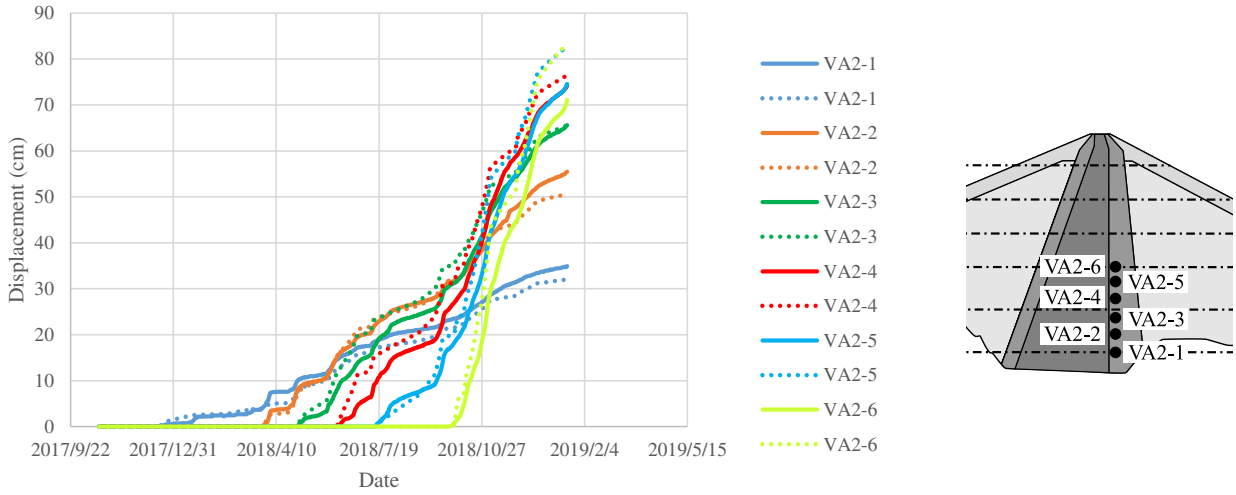


*Figure 6. Time histories of displacement (filter zone).*

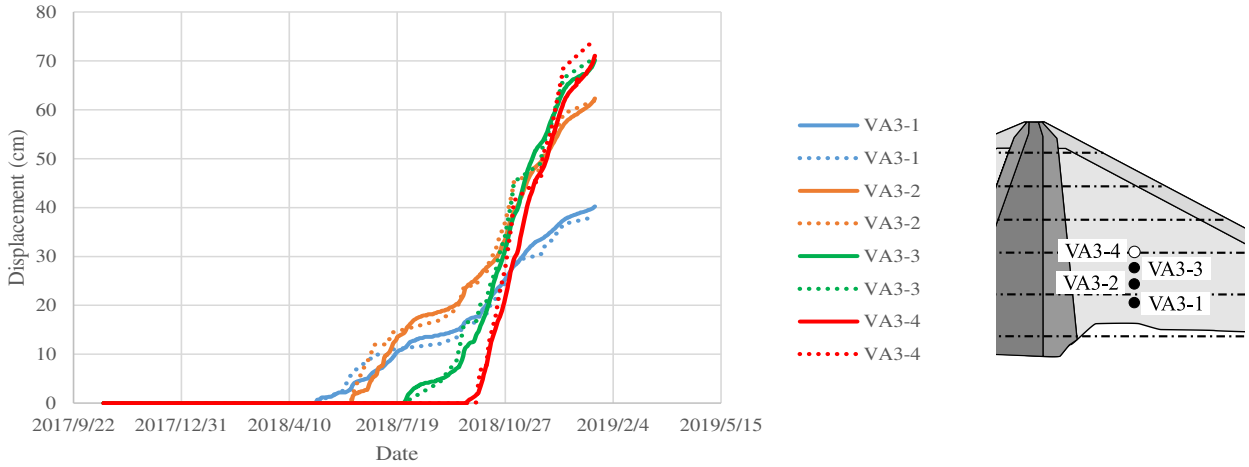


*Figure 7. Time histories of displacement (downstream rock zone).*

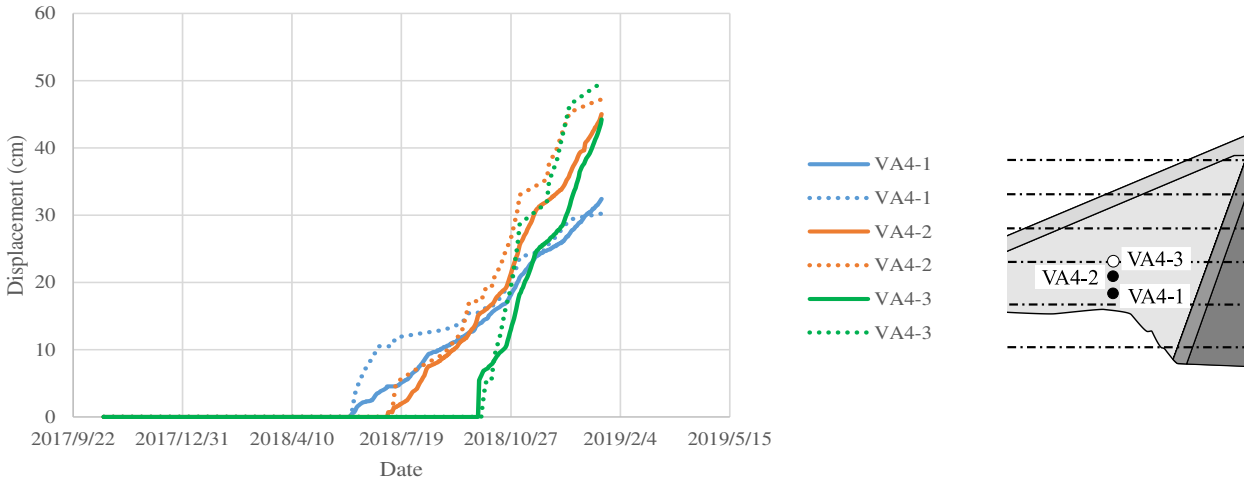


*Figure 8. Time histories of displacement (upstream rock zone).*

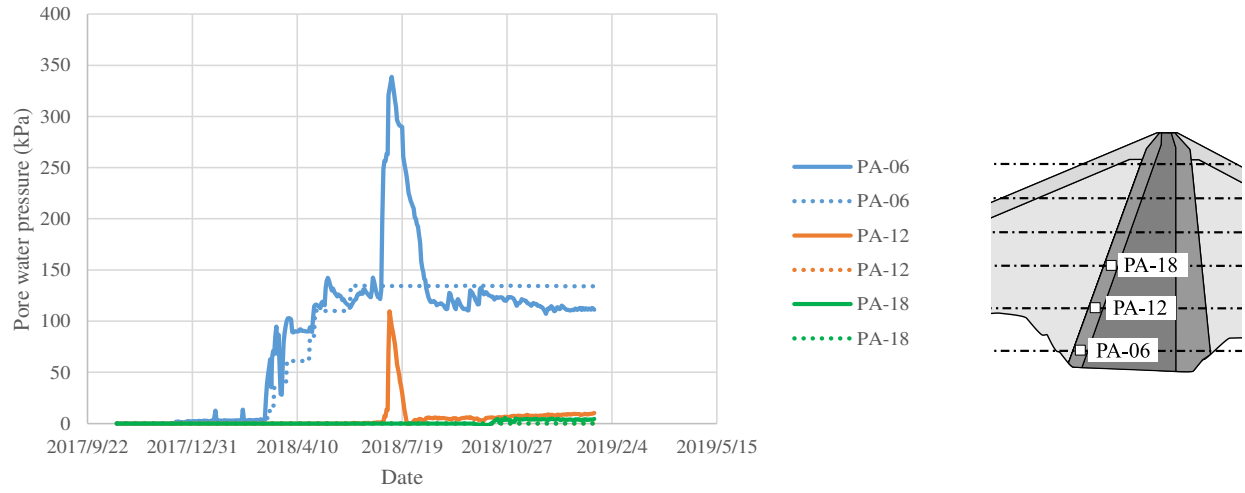


*Figure 9. Time histories of pore water pressure (upstream filter zone).*

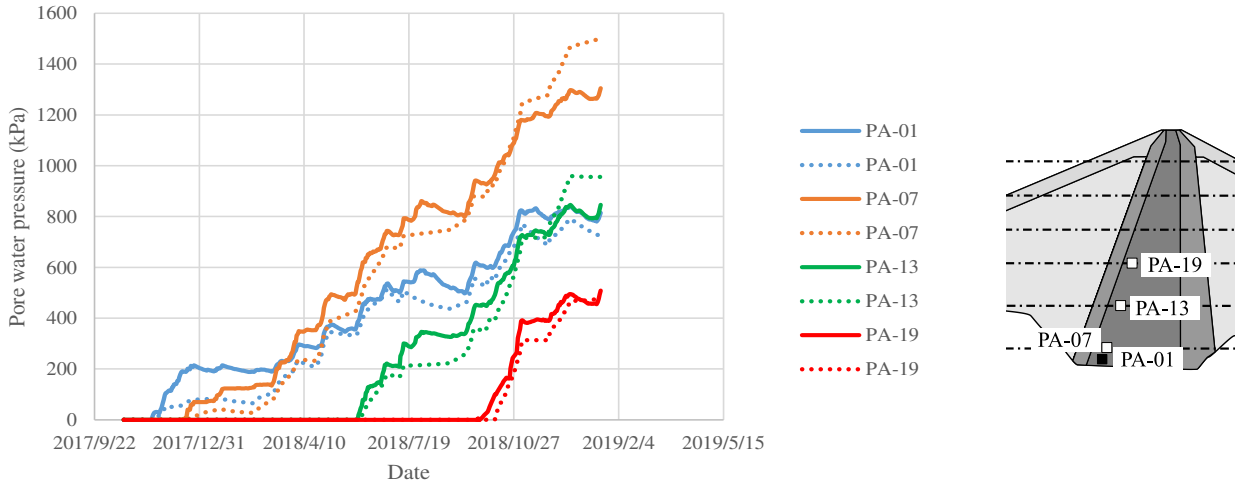


*Figure 10. Time histories of pore water pressure (upstream core zone).*

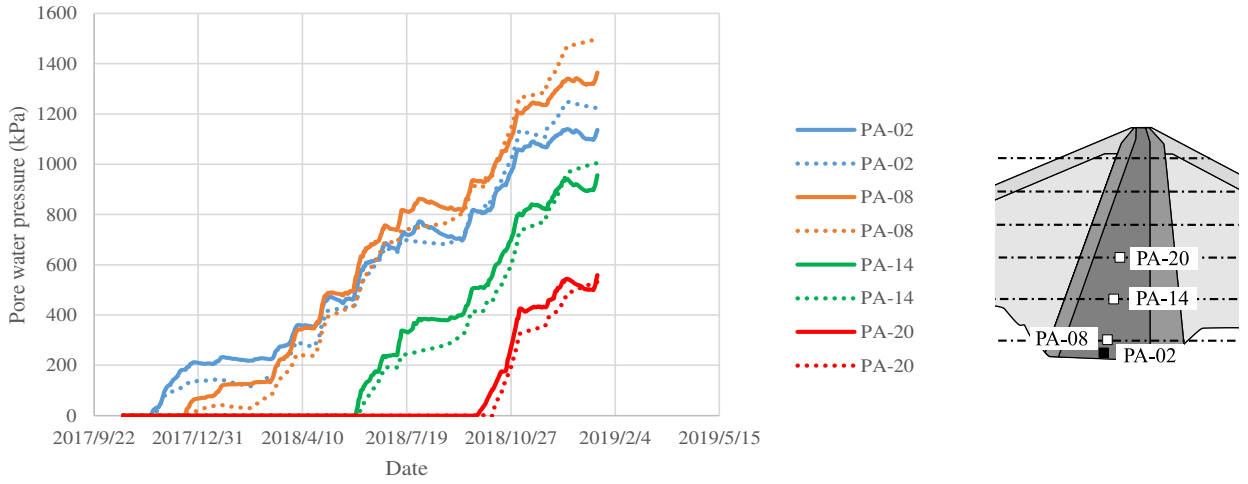


*Figure 11. Time histories of pore water pressure (center core zone).*

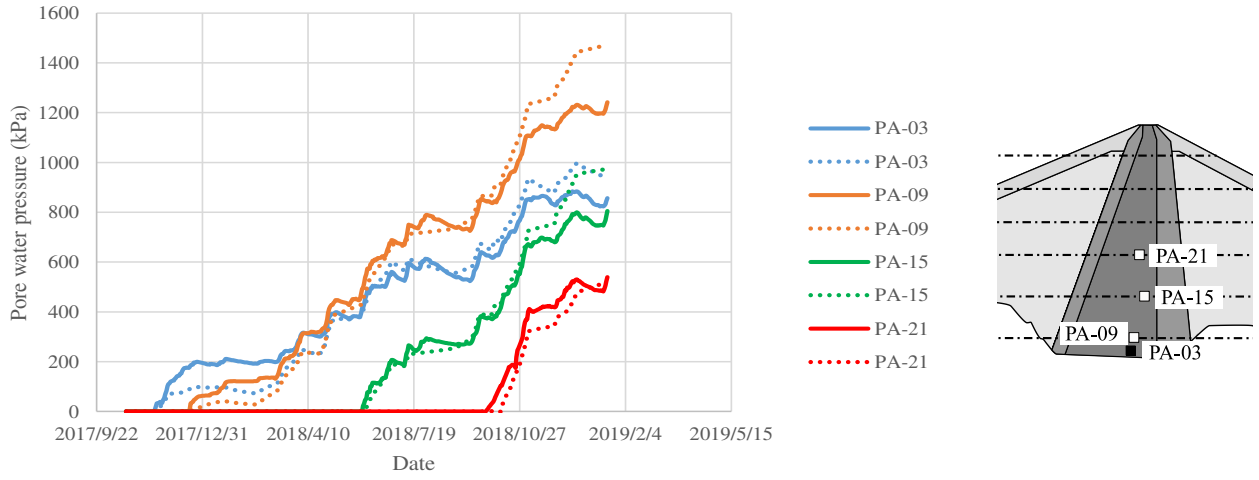


*Figure 12. Time histories of pore water pressure (downstream core zone).*

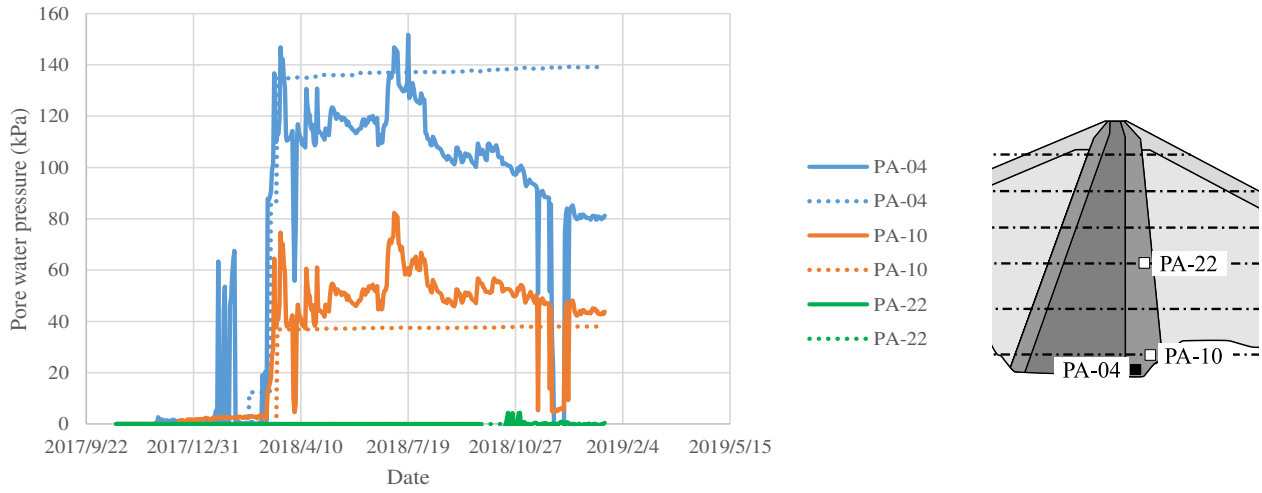


*Figure 13. Time histories of pore water pressure (downstream filter zone).*

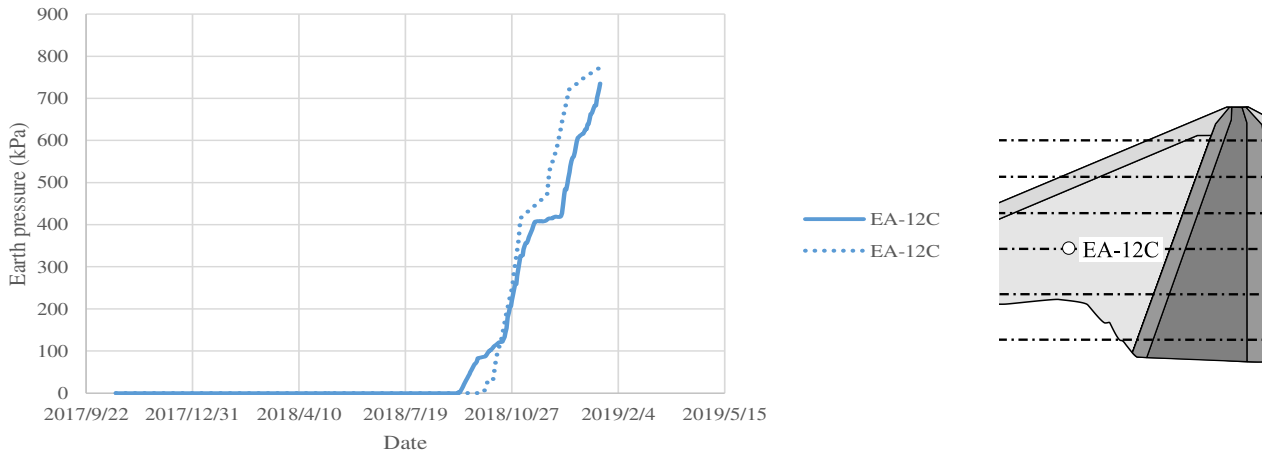


*Figure 14. Time histories of earth pressure (upstream rock zone).*

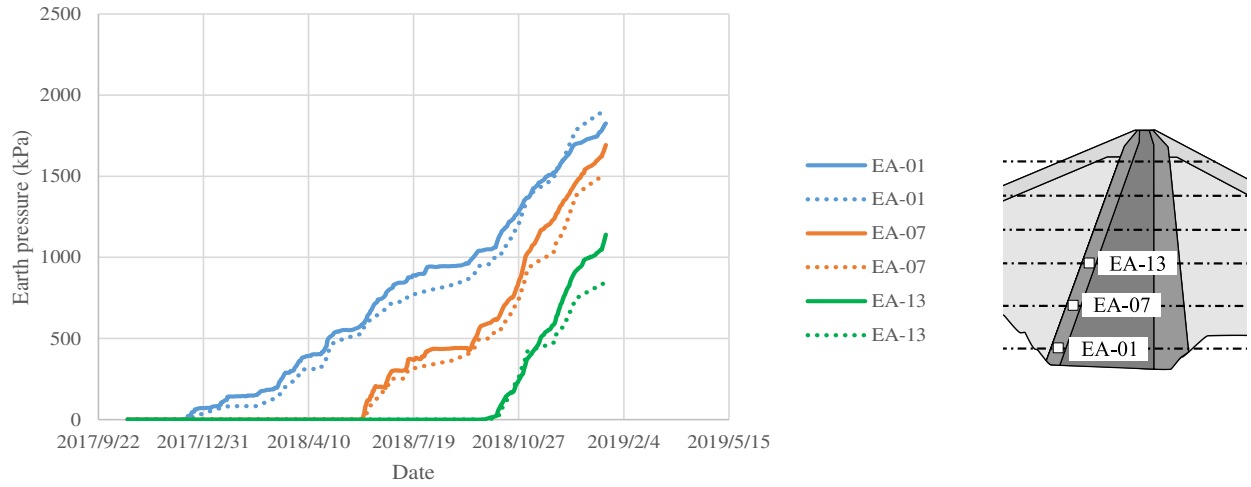


*Figure 15. Time histories of earth pressure (upstream filter zone).*

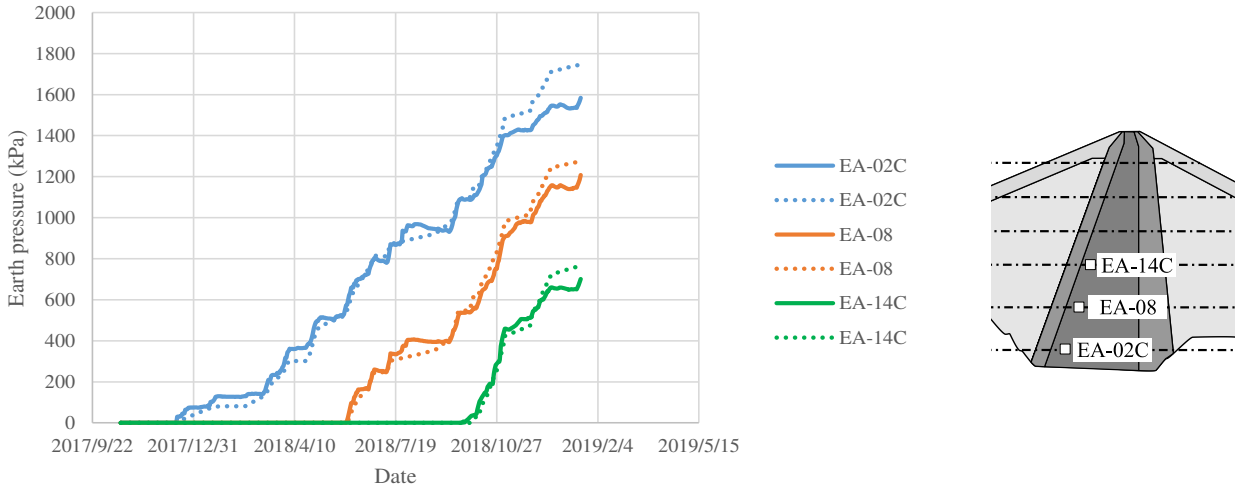


*Figure 16. Time histories of earth pressure (upstream core zone).*

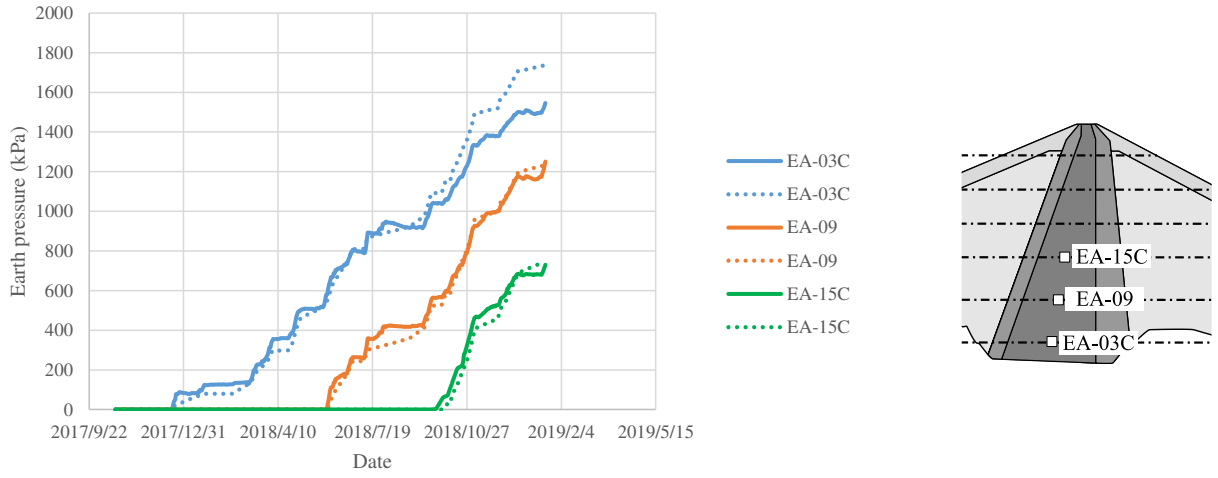


*Figure 17. Time histories of earth pressure (center core zone).*

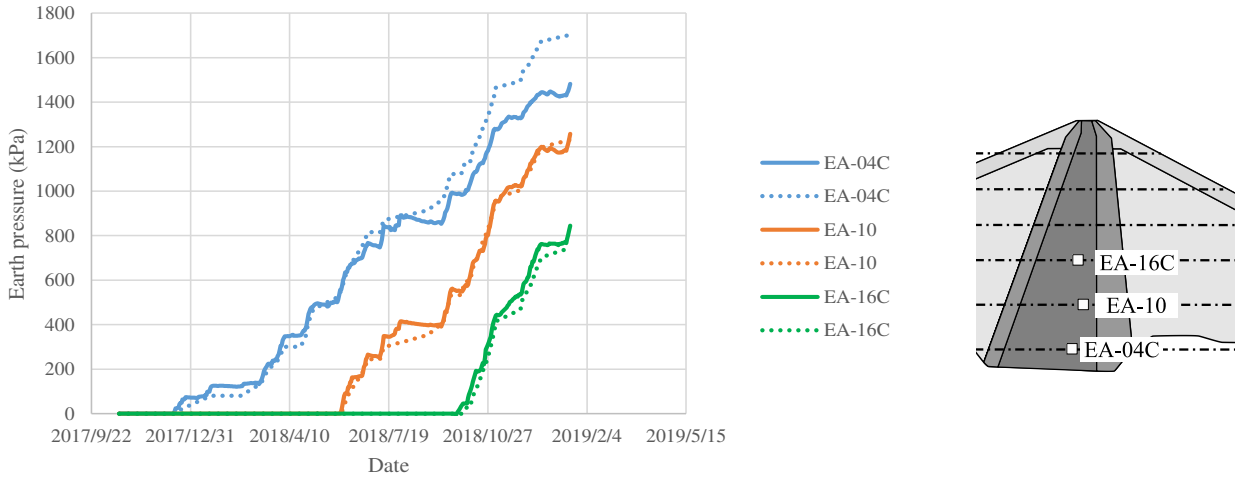


*Figure 18. Time histories of earth pressure (downstream core zone).*

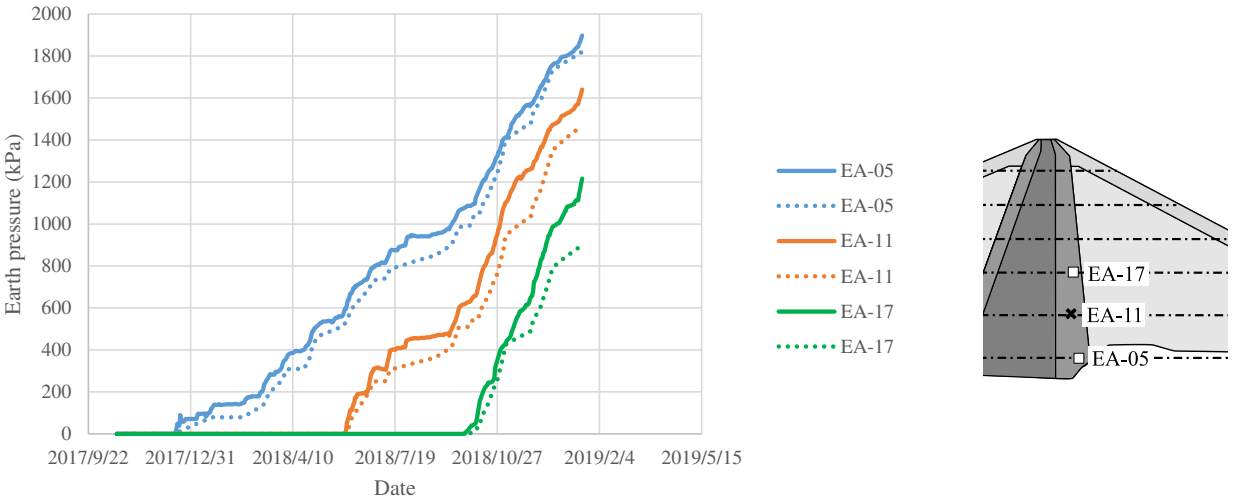


*Figure 19. Time histories of earth pressure (downstream filter zone).*

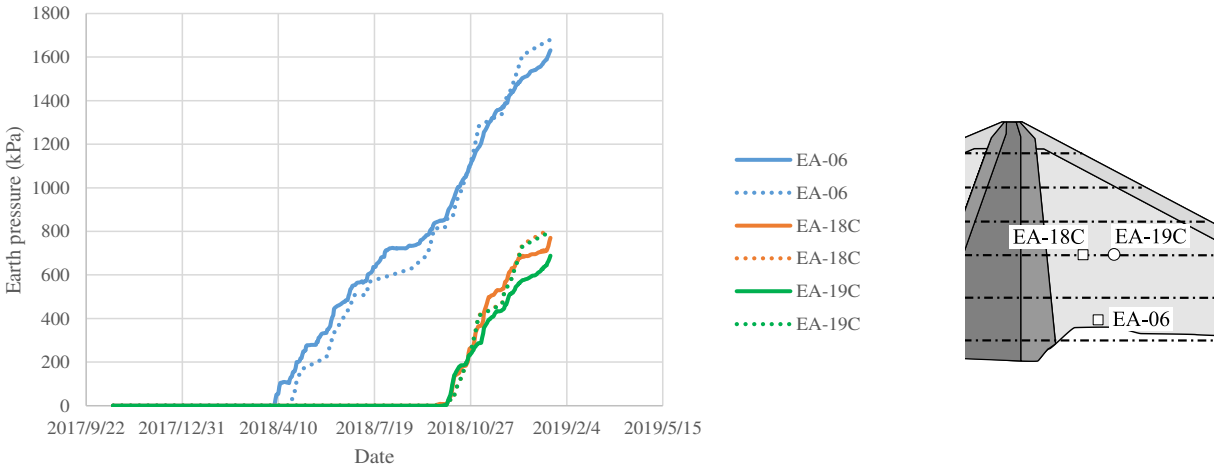


*Figure 20. Time histories of earth pressure (downstream rock zone).*

As seen in Table 4, the values of the identified parameters moderately change as the number of particles increases. The RMSE (Root Mean Square Error) is defined as:

$$\mathrm{RMSE} = \sqrt{\frac{1}{L}\sum_{i=1}^{L} {e_i}^2} \tag{19}$$

and plays an important role in the assessment of the accuracy of the numerical results shown in Figures 5-20. In Eq. (19), $e_i$ and $L$ denote the error between the observed and the computed values at the time step having the observation data, and the number of errors which is the same as the amount of observation data of interest, respectively. Figure 21 shows the relationship between the number of particles and the RMSEs of the vertical displacement, pore water pressure, and earth pressure separately. It can be seen that all of the RMSEs almost constantly decrease as the number of particles increases. In addtion to the RMSEs for each type of observation data, such as vertical displacement and pore water pressure, the following NRMSE (Normalized Root Mean Square Error) is defined as:

$$\mathrm{NRMSE} = \sqrt{\frac{1}{L}\sum_{i=1}^{L} \left(\frac{e_i}{\alpha_i S_i}\right)^2} \tag{20}$$

and considered to evaluate the total error between the numerical results and all the observation data. $\alpha_i S_i$ in Eq. (20) is the standard deviation comprising the variance/covariance matrix $R_t$ in Eq. (18), and the value of $\alpha_i S_i$ should be selected from $\alpha_1 S_1$, $\alpha_2 S_2$, … and $\alpha_{obs} S_{obs}$, depending on the observation point associated with error $e_i$. Figure 22 shows the NRMSEs calculated with all the observation data on the vertical displacement, pore water pressure, and earth pressure.

The algorithm of the PF works better for minimizing the NRMSEs between the computation and the observation as the number of particles increases because the accuracy of the posterior probabilistic distribution is enhanced. Hence, Figure 22 shows that the total NRMSEs decrease constantly as the number of particles increases, and that the PF carried out the identification of the parameters properly. In the figure, the total NRMSEs do not change significantly when the number of particles is in the range of 2,000 to 4,000, and the total NRMSEs start to decrease significantly after the number of particles exceeds 5,000. A moderate decrease in the total NRMSEs can be seen when the number of particles rises above 10,000, which implies that 10,000 particles are necessary and sufficient for this analysis. Figure 23 provides the weights $w_T^{(i)}$ (see Eq. (17)) in terms of the six parameters which have been identified. Only one peak (or mode) appears in the weight distribution of every parameter. This means that the average values given by Eq. (17) can be adopted as the identified values of the parameters.

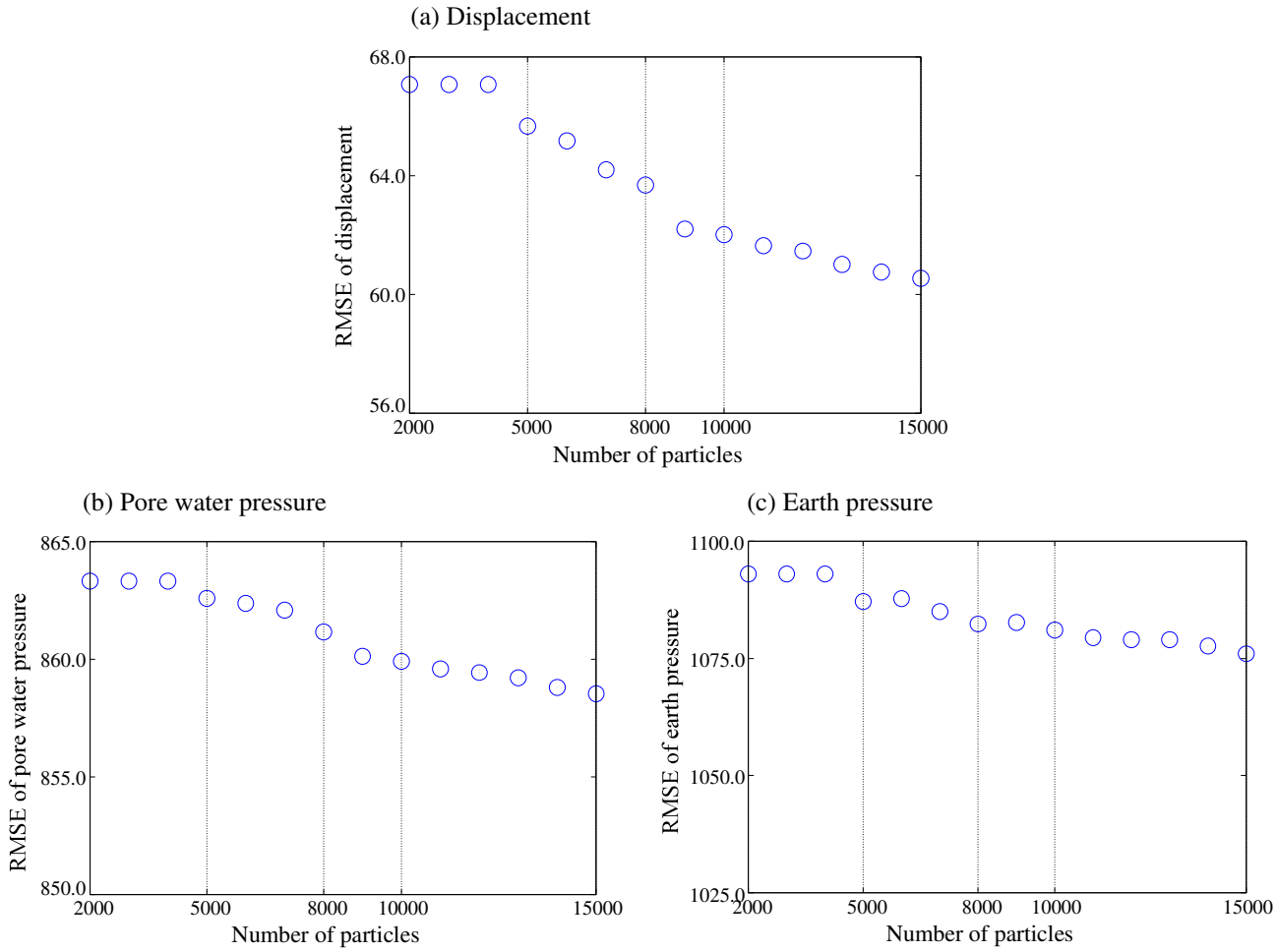


*Figure 21. RMSEs between numerical results and observation data: (a) displacement, (b) pore water pressure, and (c) earth pressure.*

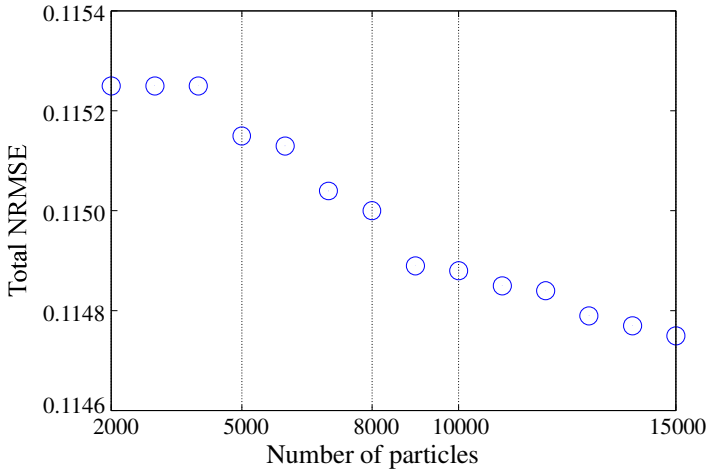


*Figure 22. Total NRMSEs of vertical displacement, pore water pressure, and earth pressure.*

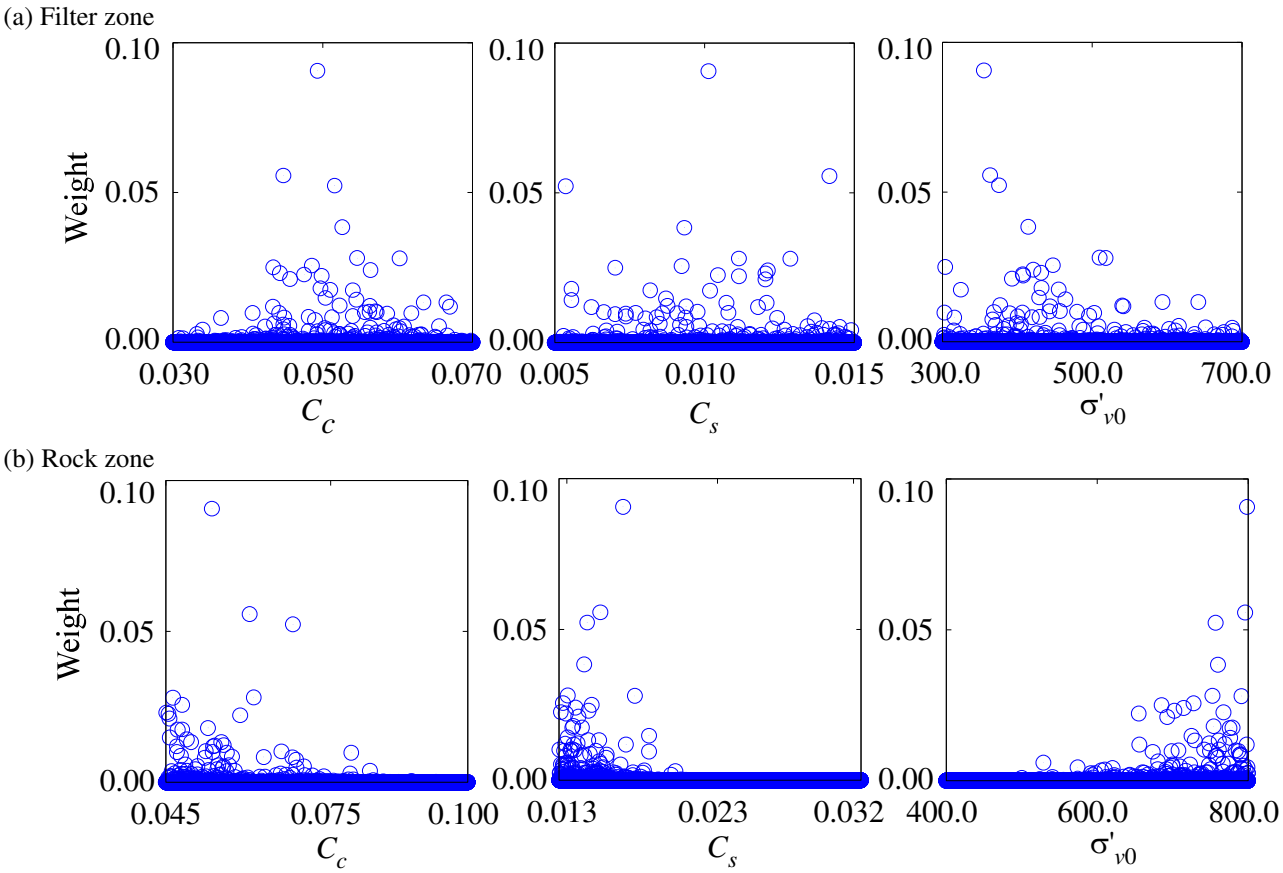


*Figure 23. Weights of identified parameters (N=10,000).*

**CONCLUSIONS**

When a rock-fill dam is constructed, the mechanical behavior of the structure, such as deformation, must be predicted so as to realize and confirm its safe construction. In order to predict the mechanical behavior, it is indispensable to know the constitutive parameters of the materials used for the construction. However, there are usually some parameters which are necessary, but not known in advance, or which are not accurate because of the significantly different conditions under which the field and the laboratory tests are conducted. On the other hand, the settlement and pore water pressure in the dam are monitored during its construction. Hence, these measured data can be utilized for the determination of the unknown parameters and the correction of any inaccurate parameters. This study has attempted to identify the material parameters of compression index $C_c$, swelling index $C_s$, and vertical yield stress $\sigma'_{v0}$ in the filter and rock zones of a real dam using the observation data obtained during its construction. The PF, which is one of the data assimilation methods, has been applied to this problem, and incorporated into the water-soil coupled FEM, for computing the deformation of the soil structure. The findings obtained and lessons learned from this case study are summarized below.

- The PF has a great advantage in that the prediction step and the filtering step are completely separated when the SIS (Sequantial Improtance Sampling) algorithm is employed. This enables the usage of any available program or software for the deformation analysis without changing the code of the program, which is quite helpful when applying the PF to the parameter identification of practical problems.

- The numerical results obtained from the identified parameters agreed surprisingly well with the measured data, which revealed the prominent applicability of the method presented in this paper to practical problems encountered in the dam construction process. This case study has provided a successful example of predicting the deformation of a dam during its construction.

- In this case study, 10,000 particles, i.e., 10,000 sets of random values of parameters to be identified, were considered to be necessary and sufficient. The relationship between the number of particles and the total NRMSEs (Normalized Root Mean Square Error) was calculated with 2,000 to 15,000 particles. The relationship suggests that the errors moderately decrease when the number of particles exceeds 10,000.

**ACKNOWLEDGMENTS**

The Japan Water Agency and Kajima Corporation supported this case study and provided the observation data. The work was also financially supported by JSPS KAKENHI Grant Number JP18H03967.

**REFERENCES**

Aydemir, A., and Güven, A. (2017). "Modified risk assessment tool for embankment dams: case study of three dams in Turkey." *Civil Engineering and Environmental Systems*, 34(1), 53-67.

Bailey, R., and Baù, D. (2010). "Ensemble smoother assimilation of hydraulic head and return flow data to estimate hydraulic conductivity distribution." *Water Resources Research*, 46, W12543.

Bhutto, A.H., Zardari, S., Bhurgri, G.S., Zardari, M.A., Bhanbhro, R., Babar, M.M., and Memon, B.A. (2019). "Parametric analysis of an embankment dam's stability." *Engineering, Technology and Applied Science Research*, 9(6), 5016–5020.

Broojerdi, M.S., Behnia, M., and Aghchai, M.H. (2018). "Dynamic analysis of rock slopes using the distinct element method: A case study at the right abutment of the Upper Gotvand Dam, Iran." *Journal of African Earth Sciences*, 145, 53-67.

Chai, T., and Draxler, R. (2014). "Root mean square error (RMSE) or mean absolute error (MAE)? –Arguments against avoiding RMSE in the literature." *Geoscientific Model Development*, 7(3), 1247-1250.

Evensen, G. (1994). "Sequential data assimilation with a non-linear quasi-geostropic model using Monte Carlo methods to forecast error statistics." *Journal of Geophysical Research*, 99, 10143–10621.

Evensen, G. (2006). *Data assimilation: The ensemble Kalman filter*, Springer, Berlin.

Gordon, N.J., Salmond, D.J., and Smith, A.F.M. (1993). "Novel approach to nonlinear/non-Gaussian Bayesian state estimation." *IEE Proceedings-F*, 140(2), 107–113.

Huang, L., Wang, L., Chen, Y., Yao Q., and Zhou. X. (2012). "The material parameter identification for functionally graded materials by the isoparametric graded finite element." *Advanced Material Research*, 446-449, 3609-3613.

Iizuka, A., and Ohta, H. (1987). "A determination procedure of input parameters in elasto-viscoplastic finite element analysis." *Soils and Foundations*, 27(3), 71-87.

Kanungo, D.P., Pain, A., and Sharma, S. (2013). "Finite element modeling approach to assess the stability of debris and rock slopes: a case study from the Indian Himalayas." *Natural Hazards*, 69, 1-24.

Kitagawa, G. (1996). "Monte Carlo filter and smoother for non-Gaussian nonlinear state space mode." *Journal of Computational and Graphical Statistics*, 5(1), 1–25.

Kodsi, S.A., Oda, K., and Awwad, T. (2018). "Viscosity effect on soil settlements and pile skin friction distribution during primary consolidation." *International Journal of Geomate*, 15(52), 152–159.

Kong, X., and Liu, J. (2002). "Dynamic failure numeric simulations of model concrete-faced rock-fill dam." *Soil Dynamics and Earthquake Engineering*, 22, 1131-1134.

Kool, J.B., Parker, J.C., and van Genuchten, M.Th. (1987). "Parameter estimation for unsaturated flow and transport models-a review." *Journal of Hydrology*, 91(3-4), 255–293, 1987.

Motesharrei, S., Rivas, J., Kalnay, E., Asrar, G.R., Busalacchi, A.J., Cahalan, R.F., Cane, M.A., Colwell, R.R., Feng, K., Franklin, R.S., Hubacek, K., Miralles-Wilhelm, F., Miyoshi, T., Ruth, M., Sagdeev, R., Shirmohammadi, A., Shukla, J., Srebric, J., Yakovenko, V.M., and Zeng, N. (2016). "Modeling sustainability: population, inequality, consumption, and bidirectional coupling of the earth and human systems." *National Science Review*, 3(4), 470-494.

Murakami, A., Shuku, T., Nishimura, S., Fujisawa, K., and Nakamura, K. (2013). "Data assimilation using the particle filter for identifying the elasto-plastic material properties of geomaterials." *International Journal for Numerical and Analytical Methods in Geomechanics*, 37, 1642-1699.

Murakami, T., Niihara, Y., Yamada, T., Ohno, S., Noguchi, T., and Miyata, M. (2012). "Prediction of horizontal deformation of large scale seawall by elasto-viscoplastic finite element analysis." *Journal of Japan Society of Civil Engineers*, 68(2), 224-238, (in Japanese).

Nakano, S., Miura, S., Parque, V., Torisaka, A., and Miyashita, T. (2019). "Data assimilation using particle filter for real-time identification of organ properties." *The 14th Asian Conference on Computer Aided Surgery (ACCAS 2018), The Journal of Engineering*, 14, 517-521.

Nguyen L.T., Nestorović, T., Fujisawa, K., and Murakami, A. (2015). "Particle filter-based data assimilation for identification of soil parameters with application in tunneling." *Proceedings of the 14th International Conference of the International Association for Computer Methods and Advances in Geomechanics (14IACMAG)*, 1241-1246.

Schaap, M.G., Leiji, F.J., and van Genuchten, M.Th. (2001). "Rosetta: a computer program for estimating soil hydraulic parameters with hierarchical pedotransfer functions." *Journal of Hydrology*, 251, 163-176.

Sekiguchi, H., and Ohta. H. (1997). "Induced anisotropy and time dependency in clays, constitutive equations of soils." *Proc. of the 9th International Conference on Soil Mechanics and Foundations Engineering*, 229-237.

Shuku, T., Murakami, A., Nishimura, S., and Fujisawa, K. (2012). "Parameter identification for cam-clay model in partial loading model tests using the particle filter." *Soils and Foundations*, 52(2), 279–298.

Sun D., Matsuoka, H., Yao, Y., and Ishii, H. (2004). "An anisotropic hardening elastoplastic model for clays and sands and its application to FE analysis." *Computers and Geotechnics*, 31, 37-46.

Takamatsu, R., Fujisawa, K., Nakahata, K., and Murakami, A. (2020). "Shape detection of multiple subsurface cavities by particle filtering with elastic wave propagation." *International Journal for Numerical and Analytical Methods in Geomechanics*, 44, 2025-2041.

Mattsson, H., Knutsson, S., and Laue, J. (2020). "Parameter identification for an embankment dam using noisy field data." *Proc. of the Institution of Civil Engineers - Geotechnical Engineering*, 173(6), 519-534.

Zhang, K., and Ai, Y. (2012). "Comparison and application of different elasto-plastic constitutive models fem analysis of an excavated soil slope." *Journal of Civil Engineering and Management*, 18(6), 802-810.

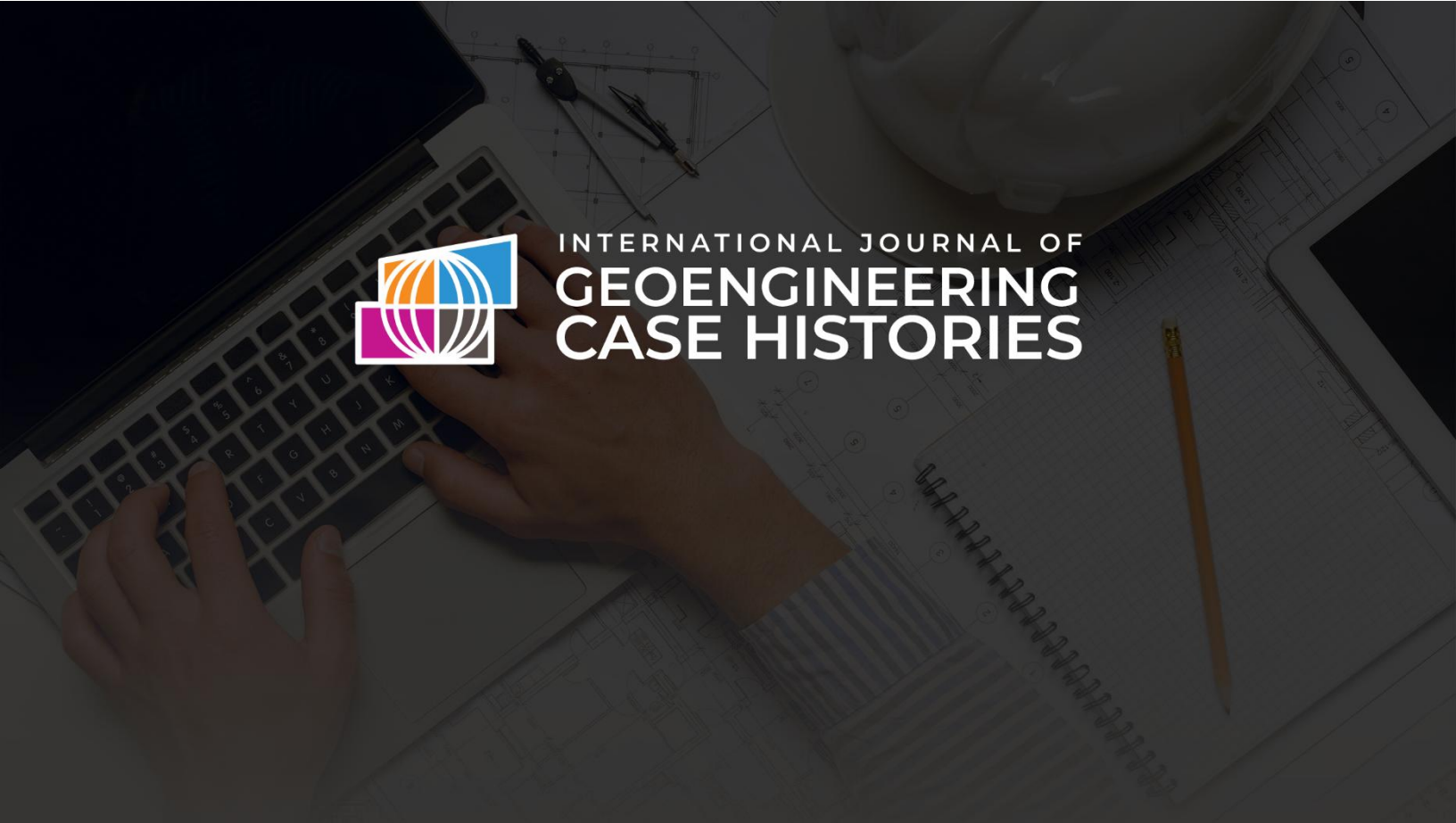

INTERNATIONAL JOURNAL OF
GEOENGINEERING
CASE HISTORIES

*The Journal's Open Access Mission is generously supported by the following Organizations:*

dar

Geosyntec consultants
engineers | scientists | innovators

ConeTec

ENGEO
Expect Excellence

*Access the content of the ISSMGE International Journal of Geoengineering Case Histories at:*
https://www.geocasehistoriesjournal.org